Pulmonary Circulation

WILEY

PVRi | Pulmonary Circulation Open Access

RESEARCH ARTICLE OPEN ACCESS

Synchrotron-Based Phase-Contrast Micro-CT Combined With Histology to Decipher Differences Between Hereditary and Sporadic Pediatric Pulmonary Veno-Occlusive Disease

Ida Jeremiasen[1,2] | Niccolò Peruzzi[1] | Elna Lampei[1,2] | Sofie Meyer[3] | Levent M. Akyürek[4] | Erik Gebre-Medhin[1] | Ceren Mutgan[5] | Peter Dorfmüller[6] | Lavinia Neubert[7,8] | Danny Jonigk[7,8,9] | Csaba Galambos[10] | Karin Tran-Lundmark[1,2]

[1]Department of Experimental Medical Science and Wallenberg Center for Molecular Medicine, Lund University, Lund, Sweden | [2]The Pediatric Heart Center, Skåne University Hospital, Lund, Sweden | [3]Department of Diagnostic Radiology, Skåne University Hospital, Lund, Sweden | [4]Department of Clinical Pathology and Cytology, Sahlgrenska Academy Hospital, Göteborg, Sweden | [5]Ludwig Boltzmann Institute for Lung Vascular Research, Graz, Austria | [6]Institute for Lung Health (ILH), Universities of Giessen and Marburg Lung Center, Giessen, Germany | [7]Institute of Pathology, Hannover Medical School, Hannover, Germany | [8]Biomedical Research in Endstage and Obstructive Lung Disease Hannover (BREATH), Hannover, Germany | [9]Institute for Pathology, RWTH Aachen University, Aachen, Germany | [10]Department of Pathology and Pediatrics, University of Colorado School of Medicine and Children's Hospital Colorado, Aurora, Colorado, USA

Correspondence: Ida Jeremiasen (ida.jeremiasen@med.lu.se)

Received: 11 June 2024 | **Revised:** 19 November 2024 | **Accepted:** 23 November 2024

Funding: This work was supported by the Swedish Heart-Lung Foundation (Hjärt-Lungfonden) (K.T.-L.), the Knut and Alice Wallenberg Foundation (Stiftelse) (K.T.-L.), the Skåne County Council Reaserch and Development Foundation, Lund, Sweden (I.J. and K.T.-L), and the Swedish Research Council (Vetenskapsrådet) (K.T.-L).

Keywords: children | *EIF2AK4* mutation | pulmonary hypertension | pulmonary veno-occlusive disease | synchrotron

ABSTRACT

Pulmonary veno-occlusive disease (PVOD) is a lethal variant of pulmonary hypertension. The degree of pulmonary arterial involvement varies. Here, we compare two PVOD patients who were transplanted at 8 years of age, whereof one is a homozygous *EIF2AK4* mutation carrier. Tissue was imaged with synchrotron-based micro-CT and the results were compared with clinical data and sectioned tissue was analyzed with histology, immunohistochemistry, immunofluorescence, and in situ hybridization. Chest CT of the noncarrier exhibited scattered poorly defined ground-glass opacities and marked septal lines, whereas the mutation carrier showed numerous nodular centrilobular ground-glass opacities and sparse septal lines. The noncarrier developed pulmonary edema with vasodilators and 3D imaging combined with histology showed severe obstruction of interlobular septal veins and medial hypertrophy of pulmonary arteries, but no arterial or arteriolar intimal fibrosis. In contrast, the mutation carrier exhibited only mild intimal fibrosis in interlobular septal veins but severe arterial and arteriolar remodeling, including intimal fibrosis, tortuous course of arterioles, muscularization extending to the alveolar duct level and multiple vascular lumens within the same pulmonary arterial adventitia. Both patients had focally thickened alveolar septa with areas of pulmonary capillary hemangiomatosis (PCH) which colocalized with increased capillary muscularization, tenascin C expression, and deposition, as well as with matrix metalloproteinase-9 (MMP9)/CD45 positive cells. In conclusion, synchrotron-based phase-contrast micro-CT is valuable for understanding vascular remodeling. Significant differences were observed between heritable and sporadic PVOD, which may influence management strategies.

1 | Introduction

Pulmonary veno-occlusive disease (PVOD) was first reported by Höra in 1934, followed by pediatric case reports in the 1960s [1, 2]. It is a rare condition with an estimated annual incidence of 0.1–0.5 cases per million and many patients are diagnosed as children or young adults [3]. In the pediatric population, PVOD has been reported to represent approximately 2% of pulmonary hypertension (PH) cases [4]. The incidence of PVOD is likely underestimated because patients are misdiagnosed as having pulmonary arterial hypertension (PAH) [3].

The World Health Organization (WHO) classifies PH into five main groups, in which Group 1 PH includes different subcategories of PAH. PVOD has been categorized as part of Group 1 since 2018, based on common hemodynamics and clinical presentations [5, 6]. However, since PVOD is characterized by significant post-capillary and capillary remodeling, it does not fully fit into Group 1. It is important to recognize and correctly diagnose PVOD because of the risk for development of significant pulmonary edema when these patients are treated for PH with pulmonary vasodilators.

The diagnostic criteria for PVOD include findings of nodular centrilobular ground-glass opacities, prominent septal lines and enlarged mediastinal lymph nodes on chest computerized tomography (CT), decreased diffusing capacity of carbon monoxide, and desaturation at rest or with exercise [7]. Studies have predominantly described adult patients and pediatric data have been limited [8, 9]. For a definite diagnosis of PVOD, a lung biopsy is needed. Specific findings typically include occlusive intimal fibrosis of pulmonary veins (PV), but also pulmonary capillary hemangiomatosis (PCH) and variable degrees of intimal fibrosis and medial hypertrophy of small pulmonary arteries (PA) [10]. Lately, PCH has been suggested to be a consequence of PVOD rather than a separate pathological process [11].

There is still some degree of uncertainty regarding specific vascular histomorphological findings in PVOD, for example, the extent of arterial changes in combination with the venous obstructions [12]. Mutations in the eukaryotic translation initiation factor 2α kinase 4 (*EIF2AK4*) gene were first described in 2014 [13]. Biallelic mutations have been reported in 13%–29% of patients with PVOD [14–16]. Differences between mutation carriers and non-carriers, for example, significantly more arterial intimal fibrosis in mutation carriers, have also been described [17]. Recent studies also imply that the bronchial circulation plays a significant role in pediatric and adult pulmonary vascular disease [18, 19], but its role in PVOD has not yet been explored in detail.

Synchrotron-based phase-contrast micro-CT has been proven a valuable tool for understanding pulmonary remodeling in three dimensions (3D) [20–23]. The pulmonary vascular microanatomy is complex and often difficult to interpret with conventional two-dimensional techniques like histology and immunohistochemistry. Recent synchrotron-based studies have led to an improved understanding of microscopic vascular changes in neonatal and adult pulmonary hypertension [20, 24].

The aim of this study was to characterize the remodeling of the distal pulmonary vasculature in 3D in sporadic versus hereditary PVOD. Two pediatric PVOD patients were studied using traditional methods, including clinical assessment, chest CT, histology, immunohistochemistry and in situ hybridization, combined with synchrotron-based phase-contrast micro-CT, a state-of the art imaging method, to describe the correlation of genotype with pulmonary vascular remodeling and clinical phenotype.

2 | Methods

2.1 | Patients and Data Collection

Two children who presented at the Pediatric Heart Center at Skåne University Hospital, Lund, Sweden, in 2017 were included in this study. Both patients were diagnosed with PVOD based on clinical presentation, imaging, hemodynamics, genetics, and response to treatment with pulmonary vasodilators. Study investigators and consultant pediatric cardiologists I.J. and K.T.-L. were involved in the assessment and care of the patients. Medical records were retrospectively reviewed and data, including age at presentation, initial symptoms, time of diagnosis, additional diagnoses, risk factors, and physical examination, were collected. The diagnostic results from electrocardiogram at presentation, blood samples, cardiac ultrasound at presentation and after treatment, chest X-ray, 6-min walk test, chest CT with contrast and/or high resolution, heart catheterization, genetics, and histopathology of explanted lungs were evaluated. For genetic analysis, a clinically established pulmonary hypertension panel, including *ACRL1* (activin A receptor-like type 1), *BMPR2* (bone morphogenetic protein receptor type 2), *CAV1* (caveolin 1), *EIF2AK4* (eukaryotic translation initiation factor 2α kinase 4), *ENG* (endoglin), *FOX1* (forkhead box F1), *KCNA5* (potassium two pore domain channel subfamily A member 5), *KCNK3* (potassium two pore domain channel subfamily K member 3), *RASA1* (RAS P21 protein activator 1), *SMAD4* (suppressor of mothers against decapentaplegic 4), and *TBX4* (T-box transcription factor 4) genes were used.

2.2 | Synchrotron-Based Phase-Contrast Micro-CT

Lung tissue obtained at the time of bilateral lung transplantation was formalin-fixed and paraffin-embedded at the Department of Pathology at Sahlgrenska University Hospital, Gothenburg, Sweden. Five paraffin blocks from each patient were studied. Propagation-based phase-contrast micro-CT was performed at the X02DA TOMCAT beamline of the Swiss Light Source at the Paul Scherrer Institute, Villigen, Switzerland and imaging of the paraffin-embedded lung tissue samples was performed as previously described [20]. In brief, standard histological staining of a top slice from each tissue block was used to guide the synchrotron imaging process by identifying areas of specific interest. Three to four areas in each block were selected and scanned. The X-ray beam was monochromatized to an energy of 21 keV. The detection system, situated at a propagation distance from the sample of 19 cm, comprised of a 20-μm-thick LuAG:Ce scintillator coupled to a ×4 magnifying objective and an sCMOS

detector. The acquisition time was set to 80 ms per projection, for a total scan time of about 2.4 min for a full scan (180°) with 1801 projections. Following image acquisition, phase retrieval was performed with Paganin's method [25]. Tomographic reconstruction was then carried out using the gridrec algorithm [26]. Each scanned volume of interest (4.2 mm × 4.2 mm × 3.5 mm, with an isotropic voxel size of 1.63 μm) was saved as a volumetric data set composed of 2160 image sections at 16-bit pixel depth.

2.3 | Image Analysis of Tomographic Scans

The CT datasets (both from the clinical scanners and from the synchrotron beamline) were visualized and analyzed with a combination of the software programs FIJI [27] (ImageJ by National Institutes of Health, Bethesda, MD, USA) and Amira (Thermo Fisher Scientific, Waltham, MA, USA).

In the case of the high-resolution clinical chest CT scans, the volumes were first processed with a median filter (3 × 3 × 3 pixel cubic structuring element) to improve the signal-to-noise ratio. Regions of interest, with a size of $4 \times 4 \times 4\ cm^3$, were then selected in comparable locations within the lungs of the two patients. In the sub-volumes, any remaining parts of the thoracic wall, which might have disturbed a rendering, were segmented and masked out. A volume rendering was then performed with the same parameters, with the aim of providing a qualitative evaluation of the structural organization of vessels, interlobular septal lines, and ground-glass opacities. No automatic distinction between these three types of structures was possible, as they presented similar gray scale values in the clinical high-resolution chest CT scans.

In the contrast-enhanced chest CT scans, the vessels were clearly distinguishable from the other features. The image quality was adequate so that a median-filtering step was not necessary. However, to further boost the visibility of the vessels, the volumes were processed with a structure enhancement filter [28]. A semi-automatic segmentation of the lung circulatory system was then obtained by using the Magic Wand tool in the Amira software. Arteries and veins were separated and visualized as surface meshes.

The synchrotron-based phase-contrast micro-CT volumes were first processed with an anisotropic diffusion filter (three iterations, with a stop threshold of 30) to improve the signal-to-noise ratio. Subsequently, the lumen of arteries, veins, and airways was segmented with a combination of the Magic Wand tool, binary image operations, and manual adjustments, all performed in Amira. The results were visualized as surface meshes.

To combine histological sections with synchrotron-based micro-CT, the histology images were first converted to grayscale by extracting only the green channel and inverting it in color (to have dark background, like in the micro-CT scans). A two-step registration was then performed. First, a 2D to 3D affine registration in Amira, using the normalized mutual information metric, identified the position of each histological section in the micro-CT volume. Then, a 2D to 2D elastic registration, performed with the FIJI plugin bUnwarpJ [29], was used to correct for the deformations that occurred during physical sectioning, rehydration, and staining, to obtain a match close to 1-to-1 between histology and corresponding micro-CT section. All the transformations performed on the grayscale histology were then extended to the original.

2.4 | Histology, Immunohistochemistry, Immunofluorescence and In Situ Hybridization

Synchrotron-based phase-contrast micro-CT is non-destructive and following imaging, the same tissue blocks could be used for histology, immunohistochemistry, and in situ hybridization to gain additional cell-specific data which could be linked to the 3D images.

Elastic van Gieson and hematoxylin and eosin (HE) stainings were performed according to standard diagnostic protocols. Immunohistochemistry for podoplanin to detect lymphatic vessels and CD34 to identify immature vascular cells were performed in an autostainer according to protocols for clinical routine by the Department of Pathology, Skåne University Hospital, Lund, Sweden. Immunohistochemistry, for tenascin C, used as a marker for vascular remodeling, von Willebrand factor (vWF), to detect both venous/venular and arterial/arteriolar endothelium, atypical chemokine receptor 1 (ACKR1), specific for venous/venular endothelium, and alpha-smooth muscle actin (αSMA), for smooth muscle cells, were done manually. ACKR1 and vWF stainings were performed as double stainings combined with αSMA. Briefly, deparaffinization and rehydration were followed by heat-induced epitope retrieval in a pressure cooker at 110°C for 5 min using Diva Decloaker (Biocare Medical, DV2004MX). Endogenous peroxidase activity was quenched with 3% H_2O_2 in tap water for 30 min. Following blocking for 20 min with 2.5% horse serum and 20 min with 10% bovine serum albumin (BSA) in phosphate buffer saline (PBS), the sections were incubated with a rabbit anti-human ACKR1 primary antibody (1:100, Thermo Fischer, PA5-82549) or a rabbit anti-human vWF primary antibody (1:1000, DAKO, A0082) for 30 min at room temperature (RT). Following washes in PBS, a secondary antibody from the horse anti-rabbit HRP polymer reagent kit (ImmPRESS Kit, Vectorlabs, MP-7401) and substrate from the ImmPACT DAB Peroxidase (HRP) substrate kit (Vectorlabs, SK-4105) were used according to the manufacturer's instructions. Following washes in PBS and another 20 min of blocking with 2.5% horse serum, a primary mouse anti-human αSMA antibody was added at a concentration of 1:500 (Abcam, ab7817) and incubated at 4°C overnight. A secondary antibody from the horse anti-mouse HRP polymer reagent kit (ImmPRESS Kit, Vectorlabs) and substrate from the Vector VIP substrate kit (Vectorlabs, SK-4600) were used according to the manufacturer's instructions. Sections were counterstained with 0.05% methyl green (Sigma, M8884-5G). Immunohistochemistry for tenascin C was also performed manually, but was done as a single staining with alkaline phosphatase-based detection. Deparaffinization, rehydration, and epitope retrieval were performed as for double stainings. Following blocking for 20 min with 2.5% horse serum, the sections were incubated with a mouse anti-human tenascin C primary antibody (1:1000, Thermo Fischer, MA5-16086) at 4°C overnight. Secondary antibody from the ImmPRESS AP horse

anti-mouse IgG Polymer kit (Vector Laboratories, MP-5402) and substrate from the ImmPACT Vector Red Substrate Kit, Alkaline Phosphatase (Vector Laboratories, SK-5105) were used according to the manufacturer's instructions. Sections were counterstained with hematoxylin. Following dehydration, slides were mounted using Pertex (HistoLab, 00840).

Multicolor immunofluorescence was conducted to identify the localization of matrix metalloproteinase 9 (MMP9). CD45 and αSMA staining were performed simultaneously on the same tissues to detect immune cells and smooth muscle cells, respectively. Deparaffinization, rehydration, and epitope retrieval were performed as described above. Following epitope retrieval, tissues were briefly rinsed with PBS and were blocked for 10 min at RT using Background Punisher (Biocare Medical, BP974). Subsequently, samples were incubated with rabbit anti-MMP9 (1:500, Abcam, ab38898), mouse anti-CD45 (1:100, [PD7/26+ 2B11], Abcam, ab781) primary antibodies at 4°C overnight. The following day, tissues were rinsed using PBS, followed by incubation for 1 h at RT with goat anti-mouse AlexaFlour 568 (1:200, Abcam, ab175701) and anti-rabbit AlexaFlour 647 (1:200, Thermo Fischer, A21246) secondary antibodies to detect CD45 and MMP9 primary antibodies. An hour of additional incubation with FITC-conjugated mouse anti-αSMA (1:200, Abcam, ab8211) primary antibody and DAPI (1:1000, Sigma, MBD0015) was performed at RT to detect smooth muscle cells and nuclei, respectively. Excess and unspecific binding was washed off between those steps using PBS. The tissues were mounted using a DAKO fluorescence mounting medium (Agilent, S3023).

In situ hybridization (ISH) for mRNA for tenascin C was performed using RNAScope (Advanced Cell Diagnostics, Newark, CA) according to the manufacturer's instructions. Briefly, 4 μm sections were deparaffinized and hybridized to the human TNC (Advanced Cell Diagnostics) probe sets using a HybEZ II oven (Advanced Cell Diagnostics) followed by use of the RNAScope 2.5 HD Detection Reagent Kit (Advanced Cell Diagnostics, 322360). Slides were mounted using Vectamount (Vectorlabs, H-5000).

All slides used for histology, immunohistochemistry, or in situ hybridization were digitalized using the Aperio ScanScope digital slide scanner (Leica Microsystems, Wetzlar, Germany). Images and scale bar references were captured in the Aperio ImageScope 12.4 (Leica Biosystems, Wetzlar, Germany) software. Immunofluorescence stainings were scanned using a Slideview VS200 (Olympus, Japan) slide scanner.

3 | Results

3.1 | Clinical Course and Management

3.1.1 | Patient 1, with No Known Mutation Found (Noncarrier)

The first patient was a 7-year-old boy who was admitted to the hospital because of episodes of chest pain, dizziness, a syncopal episode, and shortness of breath at exertion and during the night. There was no history of recent infection or cough and he had been perceived as physically healthy until 1 month before admission. Initial evaluation revealed tachycardia at 120–140 beats per minute. He had no desaturation at rest. Routine labs were negative for infections, autoimmunity, and so forth. The 6-min walking distance was 160 m (normal control > 584 m), an electrocardiogram showed signs of right ventricular hypertrophy, and echocardiography confirmed normal heart structures and no intracardiac shunt. There was evidence of moderate PH with an estimated right ventricular pressure of 80 mmHg, right heart hypertrophy, and mildly impaired function. The chest X-ray at admission showed a slightly enlarged heart, Kerley B-lines, prominent central pulmonary vessels, and a minimal right pleural effusion. A contrast-enhanced chest CT was performed at admission (described in Figure 1A). Treatment was started with diuretics, oxygen, and sildenafil. A cardiac catheterization was performed following the initiation of therapy. It revealed a mean pulmonary arterial pressure of 64 mmHg, a wedge pressure of 12 mmHg, and an indexed pulmonary vascular resistance (PVRi) of 14 wood units (WU)/m^2. With acute vasoreactivity testing, using oxygen and nitric oxide, PVRi dropped only slightly to 12 WU/m^2. Because of clinical worsening and uncertainty about the diagnosis, prostacyclin treatment was started in the intensive care unit, initially with intravenous epoprostenol which was switched to subcutaneous treprostinil after a few days. Treatment with oral bosentan was also initiated at this time and intravenous steroids were given as an extra precaution because of a slight suspicion of allergic alveolitis based on the chest CT. On this regimen, the patient initially improved but deteriorated after a few weeks. He developed significant pulmonary edema on both chest X-ray and high-resolution chest CT (HRCT, Figure 1C). Treatment was adjusted with a significant reduction of pulmonary vasodilators, an increase of diuretics and repeated pulses of steroids. A low dose of tacrolimus was also added because of the response to steroids and reports of therapeutic effects of low-dose tacrolimus in PH. Genetic testing, using a PH panel, was negative. The diagnosis of PVOD was made based on clinical symptoms by excluding other etiologies of PH and by the development of pulmonary edema following initiation of pulmonary vasodilator therapy. There was clinical improvement for 4–5 months, but his status then deteriorated with increasing oxygen demand. He then successfully underwent a lung transplantation 8 months after the initial admission, at the age of 8 years.

3.1.2 | Patient 2, Homozygous EIF2AK4 Mutation Carrier

The second patient was a 6-year-old previously healthy girl who was admitted to the hospital after 1 year of gradually increasing symptoms. She easily became exhausted during minor exertion, lost weight because of decreased appetite, and had a history of two syncopal episodes. On physical examination, she had tachycardia, 120 beats per minute, and a saturation at rest of 93%. The saturation decreased to 85% at a 6-min walk test and her walking distance was 60 m. Laboratory tests were negative for possible underlying causes like infection, autoimmunity, and liver dysfunction. Her electrocardiogram showed signs of right ventricular hypertrophy. Echocardiography confirmed normal cardiac structures and no intracardiac shunts. There was evidence of moderate PH with an enlarged right ventricle,

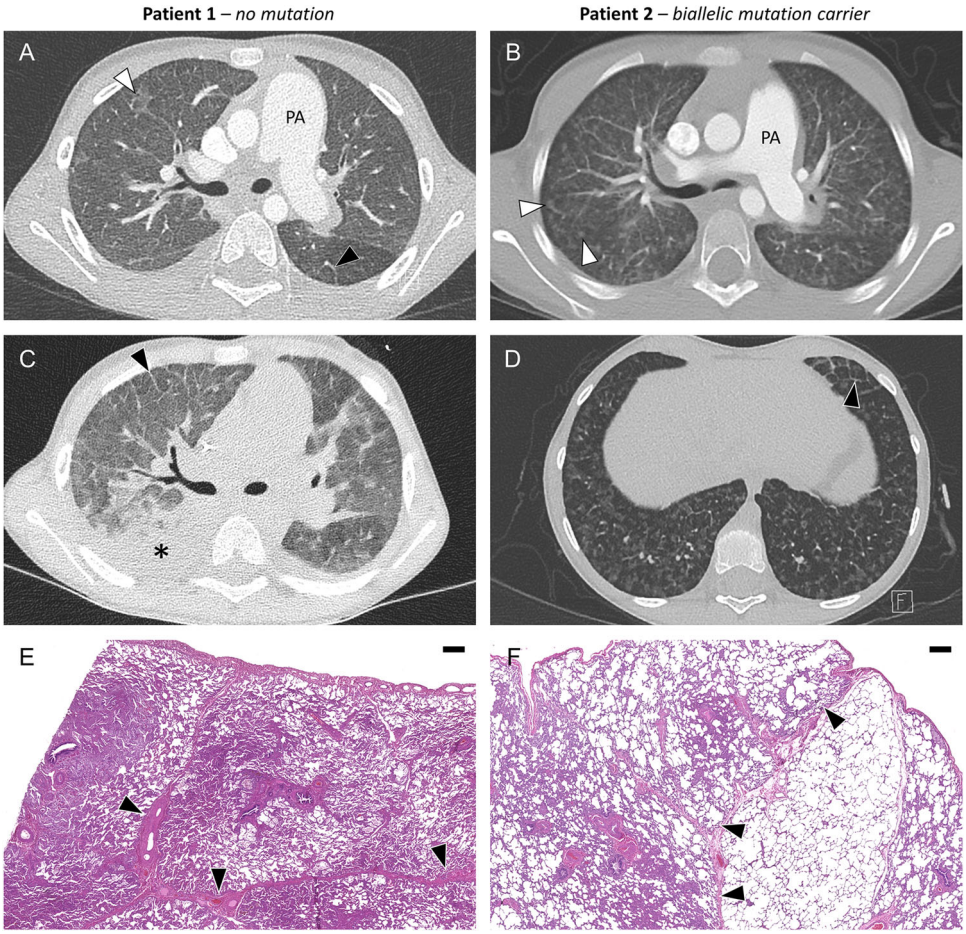

FIGURE 1 | Chest CT and histological overviews for the noncarrier patient (A, C, E) and the mutation carrier patient (B, D, F). (A) Chest CT with intravenous contrast at admission, showing thick septal lines and sparse and poorly defined ground-glass opacities. (B) Chest CT with intravenous contrast showed sparse septal lines and numerous nodular centrilobular ground-glass opacities. (C) High-resolution chest CT (HRCT) after pulmonary vasodilator therapy showed edema, more pronounced septal lines and pleural effusion. (D) HRCT at admission, at a level close to the diaphragm, where the septal lines were more prominent compared to other parts of the lung. (E) Hematoxylin and eosin staining with generally thickened alveolar walls and thickened septa and pleura. (F) Hematoxylin and eosin staining with focally thickened alveolar walls adjacent to broncho-vascular bundles and less pronounced septal thickening. Black arrowheads, septal lines; white arrowheads, ground-glass opacities. *, pleural effusion. PA, pulmonary artery. Scalebar: 400 μm.

impaired function, and an estimated right ventricular pressure of 80 mmHg. The chest X-ray at admission showed wide central PAs, marked interlobar fissures, and discrete pleural effusions. A chest CT at admission showed typical findings for PVOD with septal lines, which were quite sparse but more prominent close to the diaphragm, numerous nodular centrilobular ground-glass opacities, and enlarged mediastinal lymph nodes (Figure 1B,D). She underwent cardiac catheterization before treatment initiation. The mean pulmonary arterial pressure at baseline was 90 mmHg, and PVRi was 17.6 WU/m^2, which decreased following vasodilatation with oxygen and nitric oxide to 60 mmHg and 6.3 WU/m^2, respectively. Treatment was initiated with oxygen, diuretics, sildenafil, a calcium channel blocker, and pulse steroids. A small dose of propranolol was also added based on previously reported effects on PCH. She did not develop pulmonary edema after pulmonary vasodilator therapy, but the treatment was less aggressive compared to the first case because of the high suspicion of PVOD already at the time of treatment initiation. Tacrolimus was also added to the treatment, but there was no clear improvement. Genetic testing showed that she was homozygous for a mutation in *EIF2AK4* (c.4603_4606delAGTG, p.(Ser1535Cysfs*2)). The parents were both heterozygous carriers and there was consanguinity between them. The diagnosis of PVOD was made based on genetics in combination with the typical clinical symptoms and imaging findings. The initial symptoms improved, and the patient was treated at home for more than a year. However, her right ventricular function gradually deteriorated and she became severely hypoxic at rest and responded minimally to a combination of oxygen, diuretics, and steroids. She successfully underwent lung transplantation 1.5 years after the initial admission, at an age of almost 8 years.

Demographics, clinical investigations, and treatment courses are summarized in Table 1.

3.2 | Imaging and Histopathology Findings

Chest CT with intravenous contrast (Figure 1) of the noncarrier patient showed numerous interlobular septal lines combined with sparse, poorly defined, ground-glass opacities.

TABLE 1 | Overview of demographics, diagnostics, and treatment.

		Patient 1	Patient 2
Demographics	Gender	Boy	Girl
	Age at presentation	7 years	6 years
	Duration of symptoms at admission	1 month	1 year
	Symptoms	Syncope, chest pain, shortness of breath, dizziness	Syncope, exercise intolerance, fatigue, weight loss
Diagnostics	Chest X-ray	Wide central pulmonary arteries, Kerley B-lines, small pleural effusion	Wide central pulmonary arteries, small nodular changes, marked interlobar fissures, small pleural effusion
	Chest CT	Ground-glass opacities, septal lines, edema, small pleural effusion, some degree of lymph node enlargement	Ground-glass opacities, septal lines, lymph node enlargement
	6-MWT	160 m	125 m with O_2, 60 m without O_2, desaturation
	proBNP	5986 ng/L	4000 ng/L
	Genetic mutation	None found	*EIF2AK4* homozygous
	Cardiac catheterization	mPAP 64 mmHg, PVRi 14 WU/m^2, with NO and 100% oxygen 12 WU/m^2	mPAP 90 mmHg, PVRi 17.6 WU/m^2, with NO and 100% oxygen 6.3 WU/m^2
Treatment	Pulmonary vasodilators	Sildenafil, ilomedin, bosentan, treprostinil, epoprostenol	Sildenafil
	Oxygen	Yes	Yes
	Steroids	Pulsed	Pulsed
	Diuretics	Furosemide and spironolactone	Furosemide and spironolactone
	Propranolol	No	Yes
	Tacrolimus	Yes	Yes
Diagnosis	PVOD diagnosis	2 months after admission based on clinical diagnostics and edema following pulmonary vasodilator treatment	2 months after admission based on clinical diagnostics and genetic test result
Lung transplantation (LTx)	Listed for LTx	6 months after admission (first accepted 2 months after admission, but withdrawn because of clinical improvement)	3 months after admission
	Urgent call	Yes, for 5 days	Yes, for 1 month
	Total time on waiting list	2 months	14 months
	Age at LTx	8 years	8 years

Abbreviations: 6MWT, 6-min walk test; mPAP, mean pulmonary arterial pressure; NO, nitric oxide; proBNP, probrain natriuretic peptide; PVRi, indexed pulmonary vascular resistance; WU, wood units.

The mutation carrier underwent both chest CT with contrast and HRCT at admission. Compared to the noncarrier patient, there were fewer and more focally distributed interlobular septal lines, but more prominent and heterogeneously distributed nodular centrilobular ground-glass opacities scattered throughout the lungs. Both patients, even though more prominent in the mutation carrier, had enlarged mediastinal lymph nodes. A second HRCT showed a considerable increase in pleural fluid and edema in the noncarrier patient when triple pulmonary vasodilator therapy had been initiated. Low magnification views of hematoxylin and eosin-stained histological sections showed marked and widespread septal and alveolar wall thickening in the noncarrier patient, whereas the distribution was more scattered and patchy in

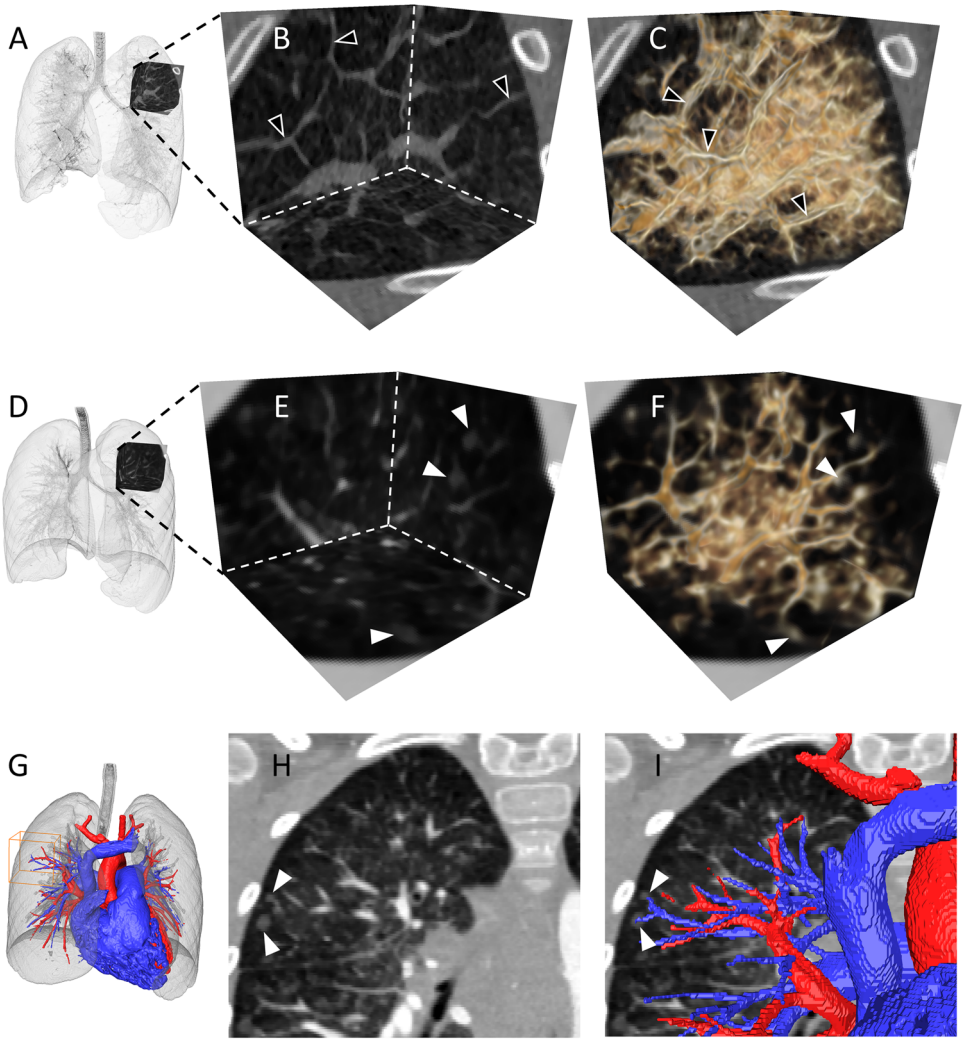

FIGURE 2 | High resolution chest CT 3D renderings of comparable areas from the left upper lobes of the two patients. (A–C) The noncarrier patient. 3D rendering with adjusted transparency of the sheet-like features that likely corresponds to "septal lines," that is, increased X-ray attenuation of the interlobular septa. (D–F) The mutation carrier patient. 3D rendering with adjusted transparency of pulmonary vessels and nodular features in close proximity to the vessels. (G–I) Magnification in 3D showing pulmonary arteries (in blue) connecting to ground-glass opacities, a finding specific for the mutation carrier patient. Black arrowheads, septal lines. White arrowheads, ground-glass opacities. Each side of the 3D box measures approximately 4 cm.

the mutation carrier, with denser areas often seen adjacent to broncho-arterial bundles and partly unaffected areas, consistent with the chest CT findings. 3D renderings of the chest CT scans (Figure 2) highlighted prominent septal lines in the noncarrier patient and ground-glass opacities in the vicinity of PAs in the mutation carrier patient.

Immunohistochemistry for podoplanin to visualize lymphatic endothelium and double staining for ACKR1 and αSMA for venous endothelium and smooth muscle identification are shown in Figure 3. The staining identified severely remodeled and often occluded veins in interlobular septa in the noncarrier patient. In the mutation carrier patient there was some degree of venous remodeling but no complete occlusions were observed. Podoplanin staining identified prominent lymphatic vessels within the interlobular septa in both patients, but also more prominent lymphatics adjacent to remodeled PAs in the mutation carrier patient (Figure 3A,B). In the noncarrier patient, the alveolar septa were thickened with dilated and muscularized capillaries and an increased airway muscularization was also observed in the walls of alveolar ducts (Figure 3C). vWF, used as control for endothelial staining, was present in both veins and arteries (brown in arterioles in insets in Figure 3C,D), whereas the ACKR1/αSMA double-staining specifically labeled the veins and confirmed severe venous remodeling. In the mutation carrier, thickened alveolar septa were also commonly observed, but with a more patchy distribution and some areas were relatively non-remodeled. Muscularization of capillaries was mainly observed adjacent to remodeled PAs and arterioles and the ACKR1/αSMA staining confirmed some degree of venous wall thickening, but the interlobular septal veins were patent (Figure 3D). Thickened arteriolar walls at the level of alveolar ducts were seen in both patients, as was increased muscularization of alveolar ducts, but the distal arteriolar changes were even more prominent in the mutation carrier. In the mutation carrier multiple lumina were also observed within the same adventitial sheath, a finding which was not observed in the noncarrier patient (Figure 3E,F). It was not possible to determine whether the arteries had been divided by newly formed walls/septations or if the vasa

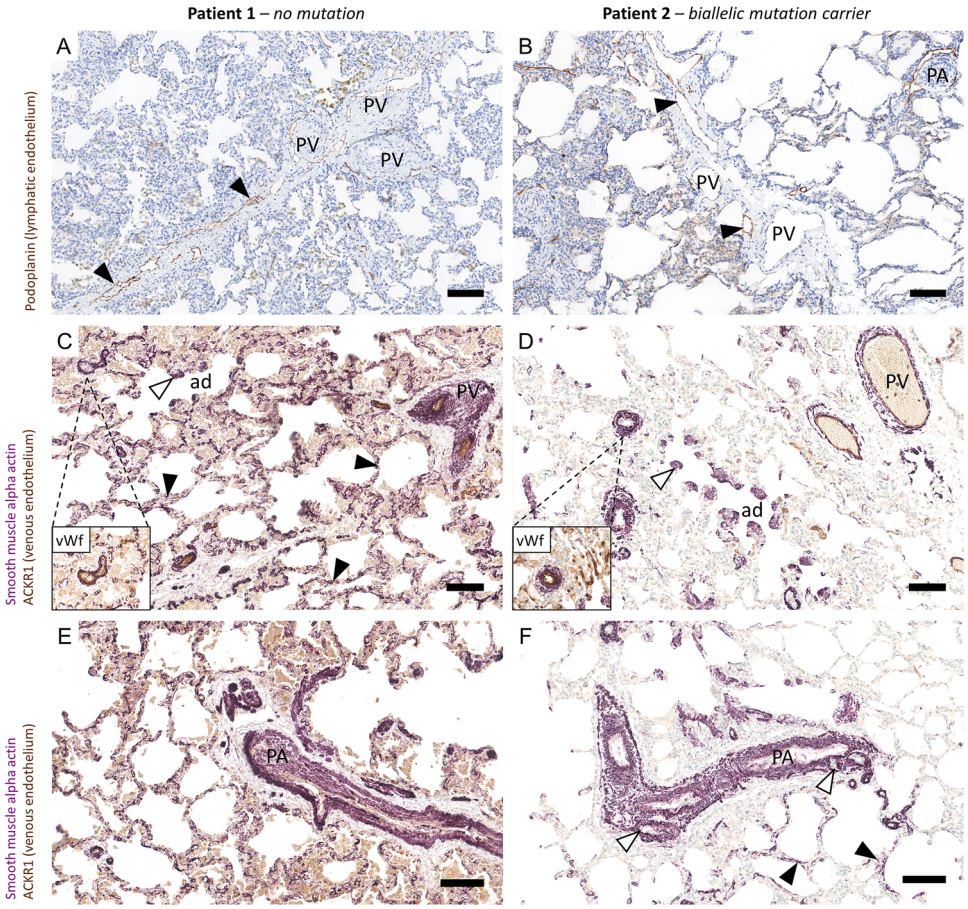

FIGURE 3 | Immunohistochemistry for the noncarrier patient (A, C, E) and the mutation carrier patient (B, D, F). (A, B) Positive podoplanin staining for lymphatic endothelium was predominantly, but not exclusively, found in the septa for the noncarrier and in the septa as well as adjacent to remodeled arteries for the mutation carrier. Black arrowheads, podoplanin in septa (brown). (C, D) Double staining with ACKR1 for venous endothelium and αSMA for smooth muscle cells illustrating differences in venous remodeling and muscularization of alveolar ducts and alveolar septa. Insets with vWF staining show the presence of endothelium in small arteries which is negative for ACKR1. White arrowheads, muscularized alveolar ducts. Black arrowheads, muscularized alveolar septa. (E, F) ACKR1/αSMA double staining showing a hypertrophied small pulmonary artery/arteriole from the noncarrier patient in (E) and in (F) an artery of similar size from the mutation carrier patient with what appears to be several lumens within the same adventitial sheath. Also, note the more sparse and patchy distribution of the capillary muscularization in the mutation carrier patient. White arrowheads, additional lumen. Black arrowheads, muscularized alveolar septa. (A–F) ad, alveolar duct; PA, pulmonary artery; PV, pulmonary vein; vWF, von Willebrand factor. Scalebar 100 μm.

vasorum, part of the bronchial circulation, had expanded by shunting.

Synchrotron-based phase-contrast micro-CT, which had been performed before sectioning the tissue, was used for 3D reconstructions of the vasculature. The multi-luminal appearance of some of the vessels in 2D histology may be the result of a tortuous course of the small and extremely hypertrophied arterioles, but this is certainly not the only explanation since dual lumens within the same adventitial sheath were confirmed in 3D (Figure 4A–D and Video S1). Patent intrapulmonary bronchopulmonary anastomoses were also observed in the mutation carrier (Figure 4E,F). Elastic van Gieson (EvG) staining (Figure 5) revealed arteries with medial hypertrophy in the noncarrier with an intact internal elastic lamina (Figure 5A). In the mutation carrier there was pronounced arterial intimal fibrosis with partly fragmented internal elastic lamina, and some degree of medial hypertrophy (Figure 5B). There was clear evidence of pulmonary venous occlusions in the noncarrier while the mutation carrier only showed mild to moderate wall thickening (Figure 5C,D). Smaller preseptal venules were also affected and partly occluded in the noncarrier patient, while preseptal venules in the mutation carrier were patent with only some intimal fibrosis (Figure 5E,F). Figure 6 shows a combination of standard histology (EvG) and synchrotron-based phase-contrast micro-CT images. In the noncarrier patient (Figure 6A,B), severely damaged and partly occluded intralobular septal veins were visualized. The PAs were patent with moderately thickened walls. The same area is also shown in Video S2. In the mutation carrier (Figure 6C,D), the PVs were patent while the PAs were severely remodeled with thick walls and narrow lumens. Arterioles could be followed with tortuous courses and clearly narrowed lumina, but without any complete occlusions observed, until the image resolution did not allow us to follow the vessels further distally. This area is also shown in Video S3. Figure 7 shows areas of prominent capillaries (PCH-like areas) in both patients, identified by EvG staining (Figure 7A,B). These areas were widespread and particularly prominent adjacent to the pleura in the noncarrier, while in the

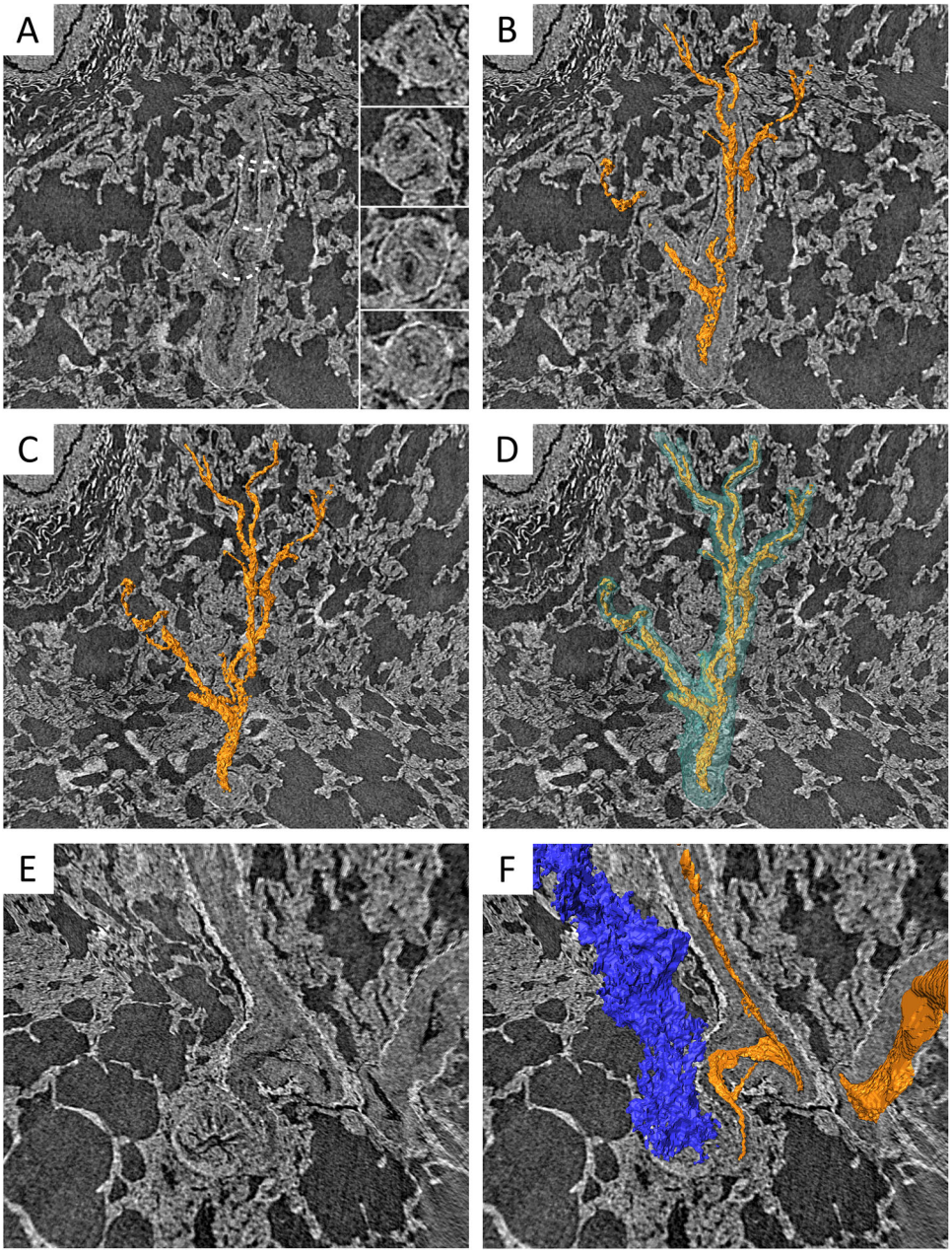

FIGURE 4 | Synchrotron-based phase-contrast micro-CT imaging of severely remodeled arterioles in the mutation carrier patient, segmented and 3D rendered. (A–D) Arteriole (yellow) with dual lumens and a tortuous course within the same adventitial sheath (transparent green in D). Insets at four levels (dotted lines) in cross-section show the multiple arterial lumens (A). (E, F) An intrapulmonary bronchopulmonary anastomosis which connects between an arteriole (yellow) and peri-bronchial vessel surrounding a bronchiole (blue) without (E) and with (F) rendering.

mutation carrier they were found scattered within the parenchyma, often adjacent to bronchoarterial bundles with severe areas with arterial remodeling. The endothelium of the PCH-affected areas stained strongly for CD34 (Figure 7C,D) and the capillary walls in these areas were markedly muscularized, as highlighted by αSMA-positive smooth muscle cells (Figure 7E,F). Expression of tenascin C mRNA and deposition of protein, as a marker for vascular remodeling and/or angiogenesis, was associated with the PCH-like areas in both patients (Figure 8A–D). MMP9 was also mainly present in leukocytes in PCH-like areas with thickened alveolar septae, and therefore more widespread in the noncarrier and patchy in the mutation carrier (Figure 8E–H). Almost no MMP9-positive leukocytes were present in the remodeled veins of either of the two patients.

The histopathology findings are summarized in Table 2.

4 | Discussion

This study describes how novel 3D imaging techniques could be combined with established histopathology, immunohistochemistry, and in situ hybridization to explore the details of vascular remodeling in PVOD. Two pediatric cases of severe PVOD were analyzed. Both patients underwent lung transplantation at the age of 8 years with similar clinical symptoms at the time of transplant. They were both severely hypoxic and responded to some extent to steroids and diuretics while on the waiting list. However, their

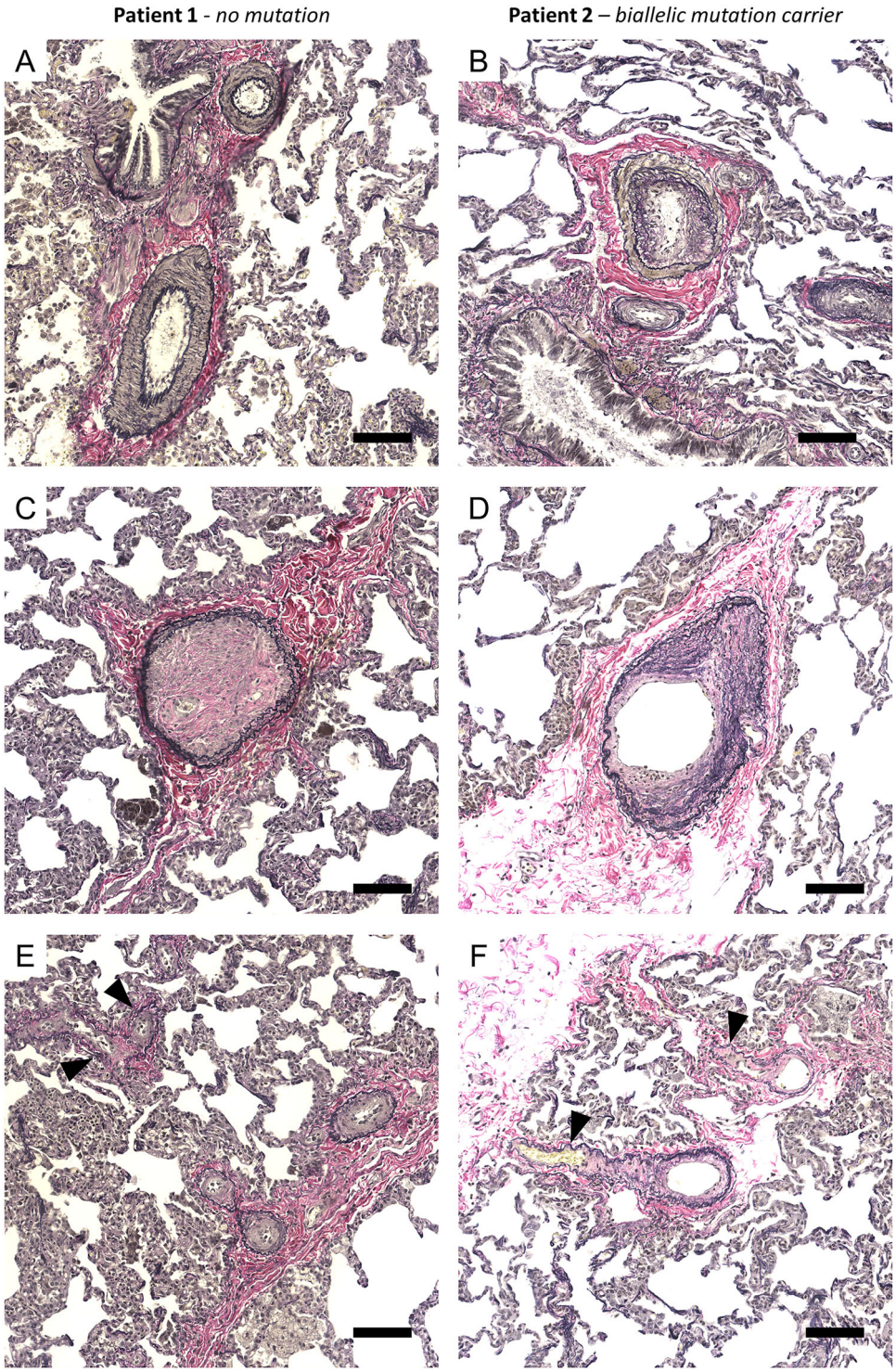

FIGURE 5 | Elastic van Gieson (EvG) staining shows vascular changes in pulmonary veins (PV) and arteries (PA) in the noncarrier patient (A, C, E) and the mutation carrier patient (B, D, F). (A) PA with medial hypertrophy and intact internal elastic lamina. (B) PA with medial hypertrophy, partly fragmented internal elastic lamina and intimal fibrosis. (C) Occluded PV. (D) Patent PV with intimal fibrosis. (E) Pre-septal venules with marked intimal fibrosis. (F) Patent pre-septal venules with minimal intimal fibrosis. Black arrowheads, pre-septal venules. Scalebar 100 μm.

disease manifestations and genetic backgrounds were different. The noncarrier patient showed a more rapid disease progression and developed pulmonary edema on pulmonary vasodilator therapy, whereas the mutation carrier suffered from a more insidious disease, the chest CT appeared more typical for PVOD, and she was found to be homozygous for an *EIF2AK4* mutation.

4.1 | Histopathology

Histological findings of PVOD have been described in numerous case reports of children since the 1960s [2]. Most of the publications of larger cohorts have also included some pediatric cases [9, 12, 17, 30]. Reported characteristic features of PVOD are intimal fibrosis of small PVs and venules

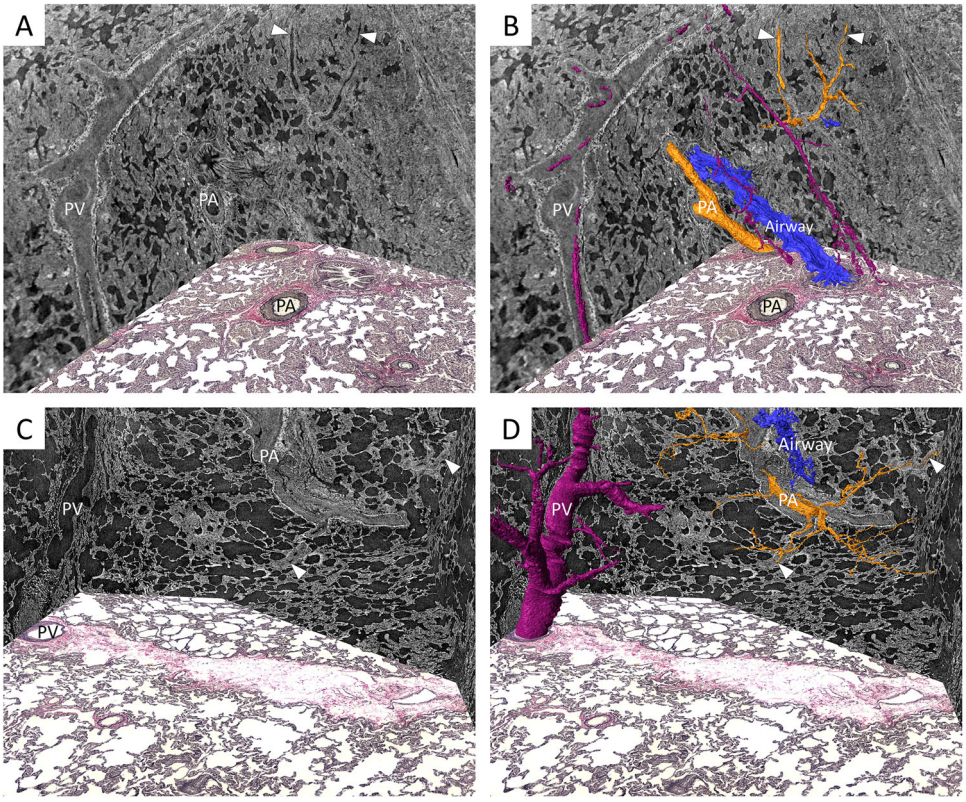

FIGURE 6 | Synchrotron-based phase-contrast micro-CT with venous (purple) and arterial (yellow) lumens segmented and 3D rendered with 2D histology (Elastic van Gieson) integrated in the 3D volumes. (A, B) The noncarrier patient with an almost occluded interlobular pulmonary septal vein (PV). Pulmonary arteries (PA) with medial hypertrophy, but patent and tortuous in the periphery. The same area is also shown in Video. (C, D) The mutation carrier patient with patent interlobular PV. PAs are severely hypertrophied. In the periphery PAs remain patent, but with narrowed lumens and a tortuous course. The same area is also shown in Video S3. White arrowheads, patent distal arteries. PA, pulmonary arteriole; PV, pulmonary vein.

and, to some extent, arterialization of veins with medial hypertrophy. The intimal fibrosis has been described as sometimes eccentric, and total obliteration of the lumen is reported as common. The same study described recanalization and formation of intravascular fibrous septa in some cases [12]. In 50% of the cohort of 26 patients studied by Wagenvoort et al., the arteries were affected in parallel with similar lesions as described for the veins above [12]. The arterial lesions were reported to be less severe in most cases, and the degree of arterial intimal fibrosis was described to vary from absent or very mild to severe [12]. There was a clear difference in the pulmonary arterial remodeling of our two patients, with mainly medial hypertrophy in the noncarrier and extensive fibrotic neointima formation in the mutation carrier patient. The results of Montani et al. suggested that non-carriers and *EIF2AK4* biallelic mutation carriers had similar chest CT and histological findings [14]. However, distinct histological differences have later been described in *EIF2AK4* mutation carriers by Nossent et al., where intimal fibrosis and less severe medial hypertrophy in PA were more prominent when compared to those of non-carriers [17], consistent with our findings. An histology study of tissue from an *EIF2AK4* mutation carrier, comparing vascular remodeling in a lung biopsy and explanted lung at the time of transplantation 8 years later, also indicated that arteriolar changes start before the venous remodeling [31].

PCH is found in most PVOD patients. In a report from 2006, Lantuéjoul et al. found capillary proliferation in 73% of PVOD cases [30]. Nossent et al. described that *EIF2AK4* mutation carriers exclusively displayed a classic patchy type of PCH, whereas half of the noncarrier patients, just like our noncarrier patient, presented with a diffuse, more extensive PCH-like remodeling [17]. Our noncarrier patient showed significantly more obstructive lesions in PV compared to the mutation carrier. All other findings in the noncarrier, including interstitial thickening of the alveolar walls, congestion of the alveolar capillaries with increased muscularization and arterial medial hypertrophy, could be secondary to the venous obstructions. The etiology of the venous obstructions in our noncarrier patient remains unclear. MMP9 has previously been found to be downregulated in PVOD compared to PAH, pulmonary fibrosis, and chronic obstructive pulmonary disease [32]. Here, almost no MMP9 nor CD45-positive leukocytes were found within remodeled veins of either of the patients. MMP9 was instead localized to CD45-positive leukocytes in areas of PCH/thickened alveolar septae. Another possible etiology would be previous phlebitis with no residual inflammation, but there was no history of previous significant infection or inflammation [30, 33] and neither had our patient been exposed to any of the known associated substances including solvents or chemotherapy [34, 35]. The PCH in the mutation carrier patient was more patchy, corroborating the findings of Nossent et al., and was often found

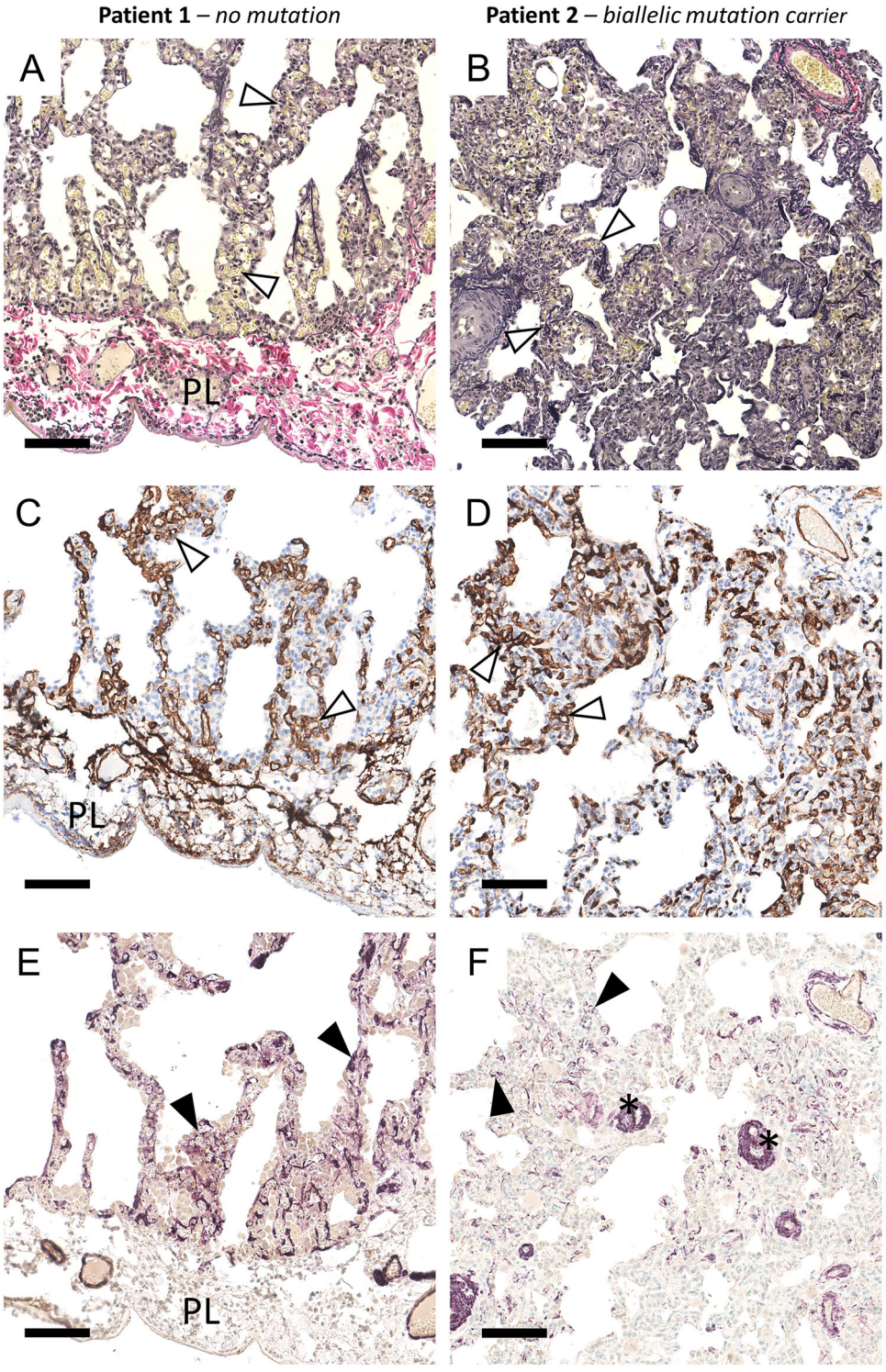

FIGURE 7 | Histology with Elastic van Gieson (EvG) to illustrate PCH-like areas and immunohistochemistry for CD34 to label activated endothelium and ACKR1/αSMA of corresponding areas to illustrate the degree of muscularization. (A) EvG, (C) CD34 (brown) and (E) αSMA (purple) for the noncarrier patient showing PCH close to the pleura with congested capillaries and increased muscularization in the same area. Some degree of PCH was present in most areas of the lung, but most pronounced in the vicinity of the pleura. (B) EvG stain, (D) CD34 (brown), and (F) αSMA (purple) for the mutation carrier patient with PCH clustered in areas adjacent to remodeled arteries/arterioles. White arrowheads, PCH areas. Black arrowheads, muscularizations. PL, pleura. *, muscularized arteriole (note the presence of dual lumen). Scalebar 100 μm.

adjacent to bronchovascular bundles where the PAs were severely remodeled. These were also the only sites where increased capillary muscularization was observed, even though thickening of alveolar septa was more widespread. Potentially the muscularization of capillaries in this case was due to redirected and increased blood flow to regions with less arteriolar remodeling. Alveolar wall thickening in some other regions may represent a sequelae of pulmonary interstitial

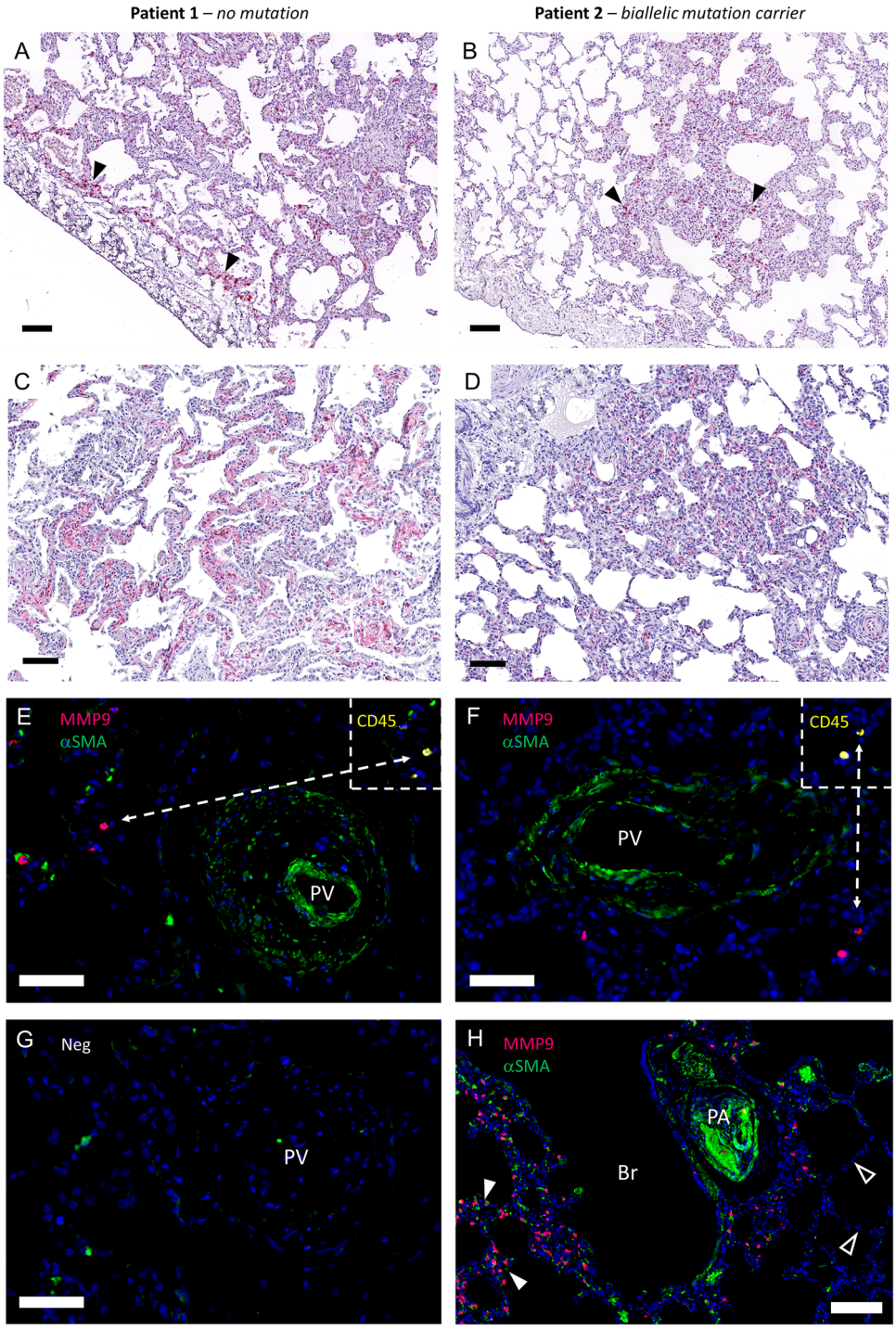

FIGURE 8 | In situ hybridization for tenascin C mRNA and immunohistochemistry for the corresponding protein, followed by triple immunofluorescence for MMP9, CD45, and αSMA. (A) Tenascin C mRNA expression (red) was, like PCH, most pronounced close to the pleura for the noncarrier patient. (B) In the mutation carrier patient, most of the tenascin C mRNA was found in areas with thickened alveolar septa adjacent to remodeled pulmonary arteries, which as in the noncarrier patient corresponded to areas of PCH. (C, D) Tenascin C protein was found in similar areas, but the difference in tenascin C mRNA between PCH areas close to the pleura and other PCH areas in the noncarrier was not observed for the protein. (E, F) Diseased veins of both patients were mostly negative for MMP9 staining. MMP9 was found in cells that also stained positive for the pan-leukocyte marker CD45, most likely lymphocytes. The insets show CD45 staining for the MMP9-positive cells. (G) Negative control (noncarrier patient) for the immunofluorescence with green autofluorescence in erythrocytes. (H) MMP9-positive cells were predominantly found in PCH-affected areas and therefore more evenly spread in the noncarrier (not shown) and concentrated to thickened alveolar septae close to diseased bronchovascular bundles in the mutation-carrier as shown in the image. Black arrowheads, tenascin C mRNA deposits. Scalebar for (A–D) 100 μm. Br, bronchiole; PA, pulmonary arterial; PV, pulmonary vein. Filled white arrowheads, thickened alveolar septae. Open white arrowheads, thin alveolar septae. Scalebar for (E–H) 50 μm.

TABLE 2 | Overview of histopathology findings.

	Patient 1	Patient 2
Veins	Complete occlusions and near complete occlusions in interlobular septal veins.	Intimal fibrosis in interlobular septal veins, but no complete occlusions.
Pulmonary arteries	Medial hypertrophy	Fibrotic neointima, muscularization, extending to the alveolar duct level. More than one lumen within the same adventitia.
PCH	Widespread. Most pronounced close to the pleura.	Patchy. Most pronounced around diseased arterioles/ bronchovascular bundles.

pneumonitis which has been reported in a patient who, like our patient, responded well to steroids [36]. Lantuéjoul et al. noted a mild interstitial lymphocytic infiltrate in 71% of their examined specimens and mild interstitial fibrosis in 47% [30]. This type of mild inflammatory infiltrate was seen in both our patients and followed the PCH distribution.

4.2 | 3D Imaging

Remodeling of veins and venules in PVOD is important to distinguish from changes in arterioles. The synchrotron-based imaging proved to be a valuable tool to confirm the histological findings and to complement them with a 3D context. A tissue scan takes only approximately 2 min and makes it possible to trace a potential venule to a septum without the need to perform laborious serial sectioning. In the mutation carrier patient, we were not able to identify any complete occlusions of veins in the interlobular septa despite detailed examination of at least four scans in each of the five imaged paraffin blocks. In the cohort examined by Lantuéjoul, 9 of the 33 PVOD patients also had no noticeable changes in veins in the interlobular septa. It is possible that there are complete, or near complete, occlusions in small parenchymal venules of our mutation carrier for which our resolution was insufficient. However, we were not able to demonstrate this clearly with histology either. Tenascin C mRNA expression and protein accumulation in PCH regions may indicate ongoing vascular remodeling and/or (neo) angiogenesis corresponding to previous studies, which have shown sprouting as well as intussusceptive angiogenesis in PVOD [37].

It would also be of interest to study a potential involvement of the bronchial circulation in the pathogenesis of PVOD in more detail. Shunting to the bronchial circulation has been demonstrated in PAH [38] and our findings of dual lumens within the same adventitial sheath and evidence of patent intrapulmonary bronchopulmonary anastomoses in the mutation carrier patient may indicate shunting to the bronchial circulation including the vasa vasorum. Previous studies have also reported angioma-like proliferation of vascular channels around diseased veins and arteries in PVOD [12]. However, some of the suspected sites of shunting in our cases turned out to be a tortuous transformation of the vessel rather than two genuinely separate lumens. Injection of a radiopaque dye would be helpful in investigating this further.

We believe that the 3D renderings of the clinical chest CT images add to the understanding of septal lines and centrilobular ground glass opacities as we, with 3D, could visualize the connection of pulmonary arterioles to the ground glass opacities and visualize the septal lines as sheet-like structures when shown in 3D, likely representing fibrosis, expanded lymphatics, and interstitial fluid. It would be even more valuable if the clinical CTs from before a transplantation could be paired with standardized tissue sampling from the explanted lung followed by synchrotron-based imaging of the same tissue.

A limitation of our study is the low number of patients and the fact that our conclusions are based on qualitative analysis of histology and imaging rather than on statistically defined measurements. However, our two patients were of similar age at the time of transplantation and presented at the same hospital, which made it reasonable to compare them considering that PVOD is very rare.

In conclusion, synchrotron-based imaging provided a unique 3D visualization of vascular remodeling in PVOD. The most striking findings of our study were the presence of prominent occlusions of interlobular septal veins in the noncarrier and the absence of these in the mutation carrier patient who instead had more arterial intimal fibrosis and an extreme muscularization of intra-acinar arterioles. The different types of vascular remodeling impacting PAs, veins, and potentially bronchial vessels seen in the noncarrier versus the *EIF2AK4* mutation carrier patient could influence management strategies in the future.

Author Contributions

K.T.-L. planned the study. I.J., N.P., E.L., S.M., E.G.M., C.M., L.A., L.N., D.J., C.G. and K.T.-L. conducted the study. All authors interpreted the results and edited the manuscript.

Acknowledgments

We acknowledge the Paul Scherrer Institute, Villigen, Switzerland, for the provision of synchrotron radiation beamtime at the TOMCAT beamline X02DA of the Swiss Light Source and Dr. Anne Bonnin and Dr. Hans Brunnström for excellent technical assistance. This work was supported by the Swedish Heart-Lung Foundation (Hjärt-Lungfonden) (K.T.-L.), the Knut and Alice Wallenberg Foundation (Stiftelse) (K.T.-L.), the Skåne County Council Reaserch and Development Foundation, Lund, Sweden (I.J. and K.T.-L), and the Swedish Research Council (Vetenskapsrådet) (K.T.-L).

Disclosure

I.J. and K.T.-L. are responsible for the overall content.

Ethics Statement

The study was approved by an institutional review board and consent was also given by the parents of the patients.

Conflicts of Interest

The authors declare no conflicts of interest.

References

1. J. Höra, "Zur Histologie der klinischen 'primären Pulmonalsklerose'," *Frankfurter Zeitschrift für Pathologie* 47 (1934): 100–108.

2. K. Weisser, F. Wyler, and F. Gloor, "Pulmonary Veno-Occlusive Disease," *Archives of Disease in Childhood* 42 (1967): 322–327.

3. D. Montani, E. M. Lau, P. Dorfmüller, et al., "Pulmonary Veno-Occlusive Disease," *European Respiratory Journal* 47 (2016): 1518–1534, https://doi.org/10.1183/13993003.00026-2016.

4. R. M. Berger, M. Beghetti, T. Humpl, et al., "Clinical Features of Paediatric Pulmonary Hypertension: A Registry Study," *Lancet* 379 (2012): 537–546, https://doi.org/10.1016/s0140-6736(11)61621-8.

5. G. Simonneau, D. Montani, D. S. Celermajer, et al., "Haemodynamic Definitions and Updated Clinical Classification of Pulmonary Hypertension," *European Respiratory Journal* 53 (2019): 1801913, https://doi.org/10.1183/13993003.01913-2018.

6. G. Kovacs, S. Bartolome, C. P. Denton, et al., "Definition, Classification and Diagnosis of Pulmonary Hypertension," *European Respiratory Journal* 64 (2024): 2401324, https://doi.org/10.1183/13993003.01324-2024.

7. A. Ogawa, Y. Takahashi, and H. Matsubara, "Clinical Prediction Score for Identifying Patients With Pulmonary Veno-Occlusive Disease/Pulmonary Capillary Hemangiomatosis," *Journal of Cardiology* 72 (2018): 255–260, https://doi.org/10.1016/j.jjcc.2018.02.009.

8. M. Pfluger and T. Humpl, "Pulmonary Veno-Occlusive Disease in Childhood—A Rare Disease Not to Be Missed," *Cardiovascular Diagnosis and Therapy* 11 (2021): 1070–1079, https://doi.org/10.21037/cdt-20-320.

9. R. W. Day, P. W. Clement, A. O. Hersh, et al., "Pulmonary Veno-Occlusive Disease: Two Children With Gradual Disease Progression," *Respiratory Medicine Case Reports* 20 (2017): 82–86, https://doi.org/10.1016/j.rmcr.2016.12.007.

10. C. A. Wagenvoort and N. Wagenvoort, "The Pathology of Pulmonary Veno-Occlusive Disease," *Virchows Archiv A, Pathological Anatomy and Histology* 364 (1974): 69–79, https://doi.org/10.1007/bf01230858.

11. J. Weatherald, P. Dorfmüller, F. Perros, et al., "Pulmonary Capillary Haemangiomatosis: A Distinct Entity?," *European Respiratory Review* 29 (2020): 190168, https://doi.org/10.1183/16000617.0168-2019.

12. C. A. Wagenwoort, N. Wagenvoort, and T. Takahashi, "Pulmonary Veno-Occlusive Disease; Involvement of Pulmonary Arteries and Review of the Litterature," *Human Pathology* 16 (1985): 1033–1041.

13. M. Eyries, D. Montani, B. Girerd, et al., "EIF2AK4 Mutations Cause Pulmonary Veno-Occlusive Disease, a Recessive Form of Pulmonary Hypertension," *Nature Genetics* 46 (2014): 65–69, https://doi.org/10.1038/ng.2844.

14. D. Montani, B. Girerd, X. Jaïs, et al., "Clinical Phenotypes and Outcomes of Heritable and Sporadic Pulmonary Veno-Occlusive Disease: A Population-Based Study," *Lancet Respiratory Medicine* 5 (2017): 125–134, https://doi.org/10.1016/s2213-2600(16)30438-6.

15. M. Eyries, D. Montani, S. Nadaud, et al., "Widening the Landscape of Heritable Pulmonary Hypertension Mutations in Paediatric and Adult Cases," *European Respiratory Journal* 53 (2019): 1801371, https://doi.org/10.1183/13993003.01371-2018.

16. M. Levy, M. Eyries, I. Szezepanski, et al., "Genetic Analyses in a Cohort of Children with Pulmonary Hypertension," *European Respiratory Journal* 48 (2016): 1118–1126, https://doi.org/10.1183/13993003.00211-2016.

17. E. J. Nossent, F. Antigny, D. Montani, et al., "Pulmonary Vascular Remodeling Patterns and Expression of General Control Nonderepressible 2 (GCN2) in Pulmonary Veno-Occlusive Disease," *Journal of Heart and Lung Transplantation* 37 (2018): 647–655, https://doi.org/10.1016/j.healun.2017.09.022.

18. C. Galambos, S. Sims-Lucas, N. Ali, J. Gien, M. K. Dishop, and S. H. Abman, "Intrapulmonary Vascular Shunt Pathways in Alveolar Capillary Dysplasia with Misalignment of Pulmonary Veins," *Thorax* 70 (2015): 84–85, https://doi.org/10.1136/thoraxjnl-2014-205851.

19. C. Westöö, C. Norvik, N. Peruzzi, et al., "Distinct Types of Plexiform Lesions Identified By Synchrotron-Based Phase-Contrast Micro-CT," *American Journal of Physiology-Lung Cellular and Molecular Physiology* 321 (2021): L17–L28, https://doi.org/10.1152/ajplung.00432.2020.

20. C. Norvik, C. K. Westöö, N. Peruzzi, et al., "Synchrotron-Based Phase-Contrast Micro-Ct as a Tool for Understanding Pulmonary Vascular Pathobiology and the 3-D Microanatomy of Alveolar Capillary Dysplasia," *American Journal of Physiology-Lung Cellular and Molecular Physiology* 318 (2020): L65–L75, https://doi.org/10.1152/ajplung.00103.2019.

21. O. Have, van der, C. Westöö, F. Ahrné, et al., "Shunt-Type Plexiform Lesions Identified in the Sugen5416/Hypoxia Rat Model of Pulmonary Arterial Hypertension Using Synchrotron-Based Phase-Contrast Micro-CT," *European Respiratory Journal* 59 (2022): 2102802, https://doi.org/10.1183/13993003.02802-2021.

22. M. Ackermann, J. C. Kamp, C. Werlein, et al., "The Fatal Trajectory of Pulmonary COVID-19 Is Driven By Lobular Ischemia and Fibrotic Remodelling," *EBioMedicine* 85 (2022): 104296, https://doi.org/10.1016/j.ebiom.2022.104296.

23. C. L. Walsh, P. Tafforeau, W. L. Wagner, et al., "Imaging Intact Human Organs With Local Resolution of Cellular Structures Using Hierarchical Phase-Contrast Tomography," *Nature Methods* 18 (2021): 1532–1541, https://doi.org/10.1038/s41592-021-01317-x.

24. C. Westöö, C. Norvik, N. Peruzzi, et al., "Distinct Types of Plexiform Lesions Identified By Synchrotron-Based Phase-Contrast Micro-CT," *American Journal of Physiology-Lung Cellular and Molecular Physiology* 321 (2021): L17–L28, https://doi.org/10.1152/ajplung.00432.2020.

25. D. Paganin, S. C. Mayo, T. E. Gureyev, P. R. Miller, and S. W. Wilkins, "Simultaneous Phase and Amplitude Extraction From a Single Defocused Image of a Homogeneous Object," *Journal of Microscopy* 206 (2002): 33–40, https://doi.org/10.1046/j.1365-2818.2002.01010.x.

26. F. Marone and M. Stampanoni, "Regridding Reconstruction Algorithm for Real-Time Tomographic Imaging," *Journal of Synchrotron Radiation* 19 (2012): 1029–1037, https://doi.org/10.1107/S0909049512032864.

27. J. Schindelin, I. Arganda-Carreras, E. Frise, et al., "Fiji: An Open-Source Platform for Biological-Image Analysis," *Nature Methods* 9 (2012): 676–682, https://doi.org/10.1038/nmeth.2019.

28. A. J. Frangi, W. J. Niessen, and M. A. Viergever, "Multiscale Vessel Enhancement Filtering," in *MICCAI1998. Lecture Notes in Computer Science*, 1496 (Berlin, Heidelberg: Springer).

29. I. Arganda-Carreras, C. O. S. Sorzano, R. Marabini, et al., *Consistent and Elastic Registration of Histological Sections Using Vector-Spline Regularization* (Springer Berlin/Heidelberg, 2006).

30. S. Lantuéjoul, M. N. Sheppard, B. Corrin, M. M. Burke, and A. G. Nicholson, "Pulmonary Veno-Occlusive Disease and Pulmonary

Capillary Hemangiomatosis; A Clinicopathologic Study of 35 Cases," *American Journal of Surgical Pathology* 30 (2006): 850–857.

31. D. Montani, P. Dorfmüller, B. Girerd, et al., "Natural History Over 8 Years of Pulmonary Vascular Disease in a Patient Carrying Biallelic EIF2AK4 Mutations," *American Journal of Respiratory and Critical Care Medicine* 198 (2018): 537–541, https://doi.org/10.1164/rccm.201802-0317LE.

32. L. Neubert, P. Borchert, H. Stark, et al., "Molecular Profiling of Vascular Remodeling in Chronic Pulmonary Disease," *American Journal of Pathology* 190 (2020): 1382–1396, https://doi.org/10.1016/j.ajpath.2020.03.008.

33. P. G. I. Stovin and M. J. Mitchinson, "Pulmonary Hypertension Due to Obstruction of the Intrapulmonary Veins," *Thorax* 20 (1965): 106–113.

34. D. Montani, E. M. Lau, A. Descatha, et al., "Occupational Exposure to Organic Solvents: A Risk Factor for Pulmonary Veno-Occlusive Disease," *European Respiratory Journal* 46 (2015): 1721–1731, https://doi.org/10.1183/13993003.00814-2015.

35. N. Kawashima, M. Ikoma, Y. Sekiya, et al., "Successful Treatment of Pulmonary Hypertension With Beraprost and Sildenafil After Cord Blood Transplantation for Infantile Leukemia," *International Journal of Hematology* 97 (2013): 147–150, https://doi.org/10.1007/s12185-012-1246-z.

36. R. J. Gilroy M. W. TeagueJr., and J. E. Loyd, "Pulmonary Veno-Occlusive Disease. Fatal Progression of Pulmonary Hypertension Despite Steroid-Induced Remission of Interstitial Pneumonitis," *American Review of Respiratory Disease* 143 (1991): 1130–1133, https://doi.org/10.1164/ajrccm/143.5_Pt_1.1130.

37. L. Neubert, P. Borchert, H. O. Shin, et al., "Comprehensive Three-Dimensional Morphology of Neoangiogenesis in Pulmonary Veno-Occlusive Disease and Pulmonary Capillary Hemangiomatosis," *Journal of Pathology: Clinical Research* 5 (2019): 108–114, https://doi.org/10.1002/cjp2.125.

38. C. Galambos, S. Sims-Lucas, S. H. Abman, and C. D. Cool, "Intrapulmonary Bronchopulmonary Anastomoses and Plexiform Lesions in Idiopathic Pulmonary Arterial Hypertension," *American Journal of Respiratory and Critical Care Medicine* 193 (2016): 574–576.

Supporting Information

Additional supporting information can be found online in the Supporting Information section.